# Classification-based material decomposition method for photon counting-based spectral radiography: Application to plastic sorting

Ting Su, Valérie Kaftandjiana, Philippe Duvauchelle, Yue-Min Zhu

# Classification-based material decomposition method for photon counting-based spectral radiography: application to plastic sorting

Ting Su[a,1], Valérie Kaftandjian[a,*], Philippe Duvauchelle[a], Yuemin Zhu[b]

[a] *Univ Lyon, INSA Lyon, Laboratoire Vibrations Acoustique, F-69621 Villeurbanne, France*
[b] *Univ Lyon, INSA Lyon, Université Claude Bernard Lyon 1, CNRS, Inserm, CREATIS UMR 5220, U1206, Lyon, France*

**Abstract**

Dual-energy X-ray radiography has been commonly used for materials separation. However, its performance is limited, especially for the separation of close materials or the identification of multiple materials. To cope with this problem, we propose to investigate the material decomposition ability of spectral radiography based on photon-counting detector. The latter having energy resolving capability can provide spectral information of several energy bins and thus enables selective imaging of multiple materials. In this framework, a classification-based patchwise regularized decomposition method was proposed to gain better differentiation between materials. It consists of performing several decompositions with reduced number of materials in the basis and classifying these decompositions using their cost function values. The results on simulations showed that, in the presence of Poisson noise, the method without classification can separate acrylonitrile-butadiene-styrene (ABS) from three kinds of flame retardants (FRs: brominated FR, chlorinated FR and phosphorus FR), but that the type of FR cannot be identified. With the classification technique, ABS and three kinds of FRs can be both separated and identified at the same time when the

*Corresponding author
*Email address:* valerie.kaftandjian@insa-lyon.fr (Valérie Kaftandjian)
[1]Author Ting Su currently work with Research Center for Medical Artificial Intelligence, Shenzhen Institutes of Advanced Technology, Chinese Academy of Sciences, Shenzhen, Guangdong 518055,14 People's Republic of China.

thickness was as large as 2 mm or 4 mm. The results on real data from physical photon-counting detector further confirm that the ABS, Br and Cl can be separated from each other.

*Keywords:* X-ray, radiography, photon-counting detector, plastic sorting

## 1. Introduction

X-ray radiography is an imaging technique that allows to view the internal structure of an object. Since the transmitted image is a 2-D projection of the 3-D object, useful information can be hidden because of physical overlapping. Dual-energy radiography using either different kVps or dual-layer detector is able to obtain two radiographs or images, one at higher energy and the other at lower energy. By making weighted subtraction of these two images [1, 2] or by performing a two-material decomposition [3], elimination of overlaying materials and enhancement of the selective target material can be achieved. Dual-energy imaging has broad applications, such as rib suppression in chest radiography in medical domain [4, 5], threat detection in security inspections [6, 7, 8] and waste sorting in industrial applications [9, 10, 11]. However, its material discrimination ability is limited and materials with close atomic number ($Z$) can barely be separated.

Thanks to the recent development of X-ray detector technology, a variety of pixelated photon-counting detectors (PCD) with imaging capability have been developped [12, 13, 14, 15]. By setting different thresholds (energy bins), each pixel of PCD is capable to either discriminate the transmitted photons corresponding to the selected energy bins, or firstly count the photons above the thresholds and then make subtraction to obtain the counts of each energy bin. With such spectral information, it is possible to set apart multiple components of the object with a single scanning and obtain improved performance in the aforementioned areas [16, 17, 18, 19, 20]. Most researches about the material decomposition ability of PCD concentrate on computed tomography (CT), called spectral CT. In the work of Schlomka *et al.* [21, 22], the measured attenua-

tion coefficients in spectral CT were decomposed into photoelectric absorption, Compton scattering and K-edge components, showing that dual contrasts can be well separated and quantified. Such K-edge technique is confined to the discrimination of high-Z materials with their K-edge inside the detection energy range. Other works [23, 24, 25, 26] considered the attenuation as a combination of several basis materials, whose distribution can therefore be quantified through decomposition process. Such approach is particularly suitable for the discrimination of lighter materials that have much lower K-edge energy beyond the detection energy range. In our previous work [27, 28], a patchwise regularized decomposition method based on basis materials combination was proposed for iron determination; the method allows iron to be quantitatively separated from calcium, potassium and water. However, potassium and calcium cannot be discriminated from each other since they have close $Z$ numbers and hence close attenuation properties. The above material decomposition methods initially proposed for CT can be applied to performing radiography, thus resulting in the so-called PCD-based spectral radiography named as spectral radiography in the following for simplicity. In the present work, we propose a new material decomposition method for spectral radiography and investigate its feasibility for plastic sorting.

Waste electrical and electronic equipment (WEEE) has been increasing rapidly due to the development of electronic industry. In European Union, the amount of WEEE generated in 2005 is 9 million tons and this number is supposed to grow to 12 million by 2020 [29]. WEEE covers a wide variety of products such as lamps, hairdryers, computers, TV-sets, fridges and cell phones. This kind of waste contains various compositions among which polymers play an important part [30]. Acrylonitrile-butadiene-styrene (ABS) is a major component among all the polymers. Due to the presence of electronic power of EEE, the plastic materials should meet high fire safety standards. However, this is not possible to realize with pure polymers, therefore flame retardant (FR) are added to change flammability of plastics and increase the fire resistance [31]. Halogenated organic compounds (e.g., brominated aromatic compounds, chlorinated paraffins

and alicyclic compounds) and phosphorus compounds (e.g. organophosphates, halophosphates, phosphine oxides and red phosphorus) are two important FRs [32]. Recycling of plastics from WEEE is challenging because of the existence of FRs (especially the brominated and chlorinated FRs), which might result in serious environmental pollution. Therefore, sorting technique is important for subsequent treatment and recycling of WEEE to avoid major environmental and health problems. As mentioned before, some researches using dual-energy radiography for waste management have been reported. For example, Montagner *et al.* [9] showed that heavy FR containing bromine (Br) is easier to be detected, but that chlorinated (Cl) FR can be sorted in the same family as Br, while the lighter one containing phosphor (P) remains undetectable when material thickness is less than 10 mm. To overcome these limitations, PCD-based spectral radiography appears an interesting solution due to its ability of decomposing multiple components of an object with a single scanning.

The purpose of the present work is to investigate the method of material decomposition for spectral radiography to discriminate plastic material from several FRs and further identify the type of FR. Based on our preliminary results reported in the ECNDT 2018 conference [33], the present paper aims to propose a new material decomposition method, which consists of performing several decompositions with reduced number of materials in the basis and classifying these decompositions using their cost function values. Both simulation and experimental results will be demonstrated.

This paper reuses a substantial part from one of the co-author's own thesis [28] with permission. More precisely, the reused contents appear mainly in sections I to IV and in Appendix.

## 2. Classification-based decomposition method

In our previous work [27], a patchwise regularized decomposition (PRD) method has been proposed, which divides the projection images into small patches and performs decomposition on each patch. The limitation of this

method is to distinguish materials with close properties, and the performance of decomposition decreases when increasing the number of materials in the basis. To cope with the difficulty, the idea here is to perform several decompositions with reduced number of materials in the basis and classify these decompositions using their cost function values, thus leading to the so-called classification-based PRD (CPRD) method.

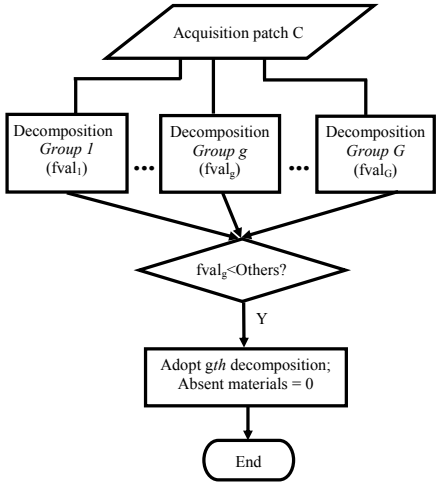


Figure 1: Flowchart of the decomposition method with classification for one patch. $\text{fval}_g$ represents the cost function value obtained by the g*th* decomposition with basis materials of *Group g*.

CPRD method also works in the way of patch-by-patch decomposition, but for several groups of materials. Figure 1 illustrates the procedure of this method for one patch. The principle is to firstly choose several groups of basis materials ( *Group 1, Group 2, ... Group g, ..., Group G*), in which the same material can belong to several groups. Then, for each patch, we perform $G$ times decomposition by carrying out PRD on each of basis material groups. For a *Group g*, the output is a set of decomposed density integrals at each pixel of the patch and a unique cost function value. After this step, we select the basis material group having the smallest cost function and we adopt the set of concentration values obtained from the decomposition based on this basis material group, while the

concentration of other materials inside this patch are set to 0. Finally, by repeating the above procedure for all the patches, we obtain the final image of each material.

More precisely, we consider the attenuation $\mu(\overrightarrow{x}, E)$ as a combination of $M$ basis materials, where $\overrightarrow{x}$ represents location and $E$ represents energy. The basis materials can be chosen according to the prior knowledge of the scanned objects. We then have:

$$\mu(\overrightarrow{x}, E) = \sum_{\alpha=1}^{M} \rho_\alpha(\overrightarrow{x})\mu_{m\alpha}(E), \tag{1}$$

where $\rho_\alpha(\overrightarrow{x})$ denotes the density of material $\alpha$ at point $\overrightarrow{x}$ and $\mu_{m\alpha}(E)$ the mass attenuation coefficient of material $\alpha$ at energy $E$. According to Beer-Lambert law, the expected number of photons $\lambda_i$, in energy bin $B_i (i = 1, 2...N, N$ is the total number of energy bins) can be expressed as:

$$\begin{aligned}
\lambda_i &= \sum_{E=E_s(i)}^{E_f(i)} D(E)N_0(E)exp[-\int \mu(\overrightarrow{x}, E)\, ds] \\
&= \sum_{E=E_s(i)}^{E_f(i)} D(E)N_0(E)exp[-\int \sum_{\alpha=1}^{M} \rho_\alpha(\overrightarrow{x})\mu_{m\alpha}(E)\, ds] \\
&= \sum_{E=E_s(i)}^{E_f(i)} D(E)N_0(E)exp[-\sum_{\alpha=1}^{M} \mu_{m\alpha}(E)P_\alpha(sx, sy)],
\end{aligned} \tag{2}$$

with

$$P_\alpha(sx, sy) = \int \rho_\alpha(\overrightarrow{x})\, ds, \tag{3}$$

where $E_s(i)$ and $E_f(i)$ denote respectively the start and final energies of bin $B_i$, $D(E)$ is the detector absorption efficiency, $N_0(E)$ is the number of photons in the initial spectrum at energy $E$, and $P_\alpha(sx, sy)$ is the density integral that is line integral of object density $\rho_\alpha(\overrightarrow{x})$ along the measured projection path, with $(sx, sy)$ representing the index of detector pixels.

To estimate $P_\alpha(sx, sy)$, we build an objective function that combines the log-least squares [34, 35], and a regularization term $R(P_\alpha^C)$ for each small patch $C$ on the attenuation image to reduce the effect of noise and enforce smoothness:

$$P_{\alpha}^{C}(sx,sy) = \arg \min_{P_{\alpha}^{C}(sx,sy)} \{ \sum_{(sx,sy)\in C} \sum_{i=1}^{N} [\ln(\lambda_i(P_{\alpha}^{C})) - \ln(m_i^C)]^2 + rR(P_{\alpha}^{C})\}, \quad (4)$$

where $m_i^C$ is the measured number of photons in energy bin $B_i$ and within patch $C$. $r$ denotes the relaxation parameter. $R(P_{\alpha}^{C})$ is the sum of the $L2$ regularizations of gradient images of $P_{\alpha}^{C}$:

$$\begin{aligned} R(P_{\alpha}^{C}) &= \sum_{\alpha=1}^{M} || \bigtriangledown P_{\alpha}^{C} ||_2^2 \\ &= \sum_{\alpha=1}^{M} \sum_{\substack{(sx,sy)\in C \\ (sx-1,sy)\in C \\ (sx,sy-1)\in C}} \{[P_{\alpha}^{C}(sx,sy) - P_{\alpha}^{C}(sx-1,sy)]^2 \\ &\qquad + [P_{\alpha}^{C}(sx,sy) - P_{\alpha}^{C}(sx,sy-1)]^2\}. \end{aligned} \quad (5)$$

## 3. Description of the spectral radiography simulation

We use the Virtual X-ray Imaging (VXI) software [36], which was developed in INSA Lyon, to simulate spectral radiography imaging. This software allows to define multiple parameters of the object to scan, including X-ray source, detector and system geometry.

Table 1: Components of three ABS-FR materials used for the phantom.

| Material(ABS-FR) | ABS-TBBPA | ABS-DDC-CO | ABS-RDP |
|---|---|---|---|
| Density of material $\rho$(mixture) | 1060 mg/cm$^3$ | 1060 mg/cm$^3$ | 1060 mg/cm$^3$ |
| Chemical formula of FR | $C_{15}H_{12}Br_4O_2$ | $C_{18}H_{12}Cl_{12}$ | $C_{30}H_{24}O_8P_2$ |
| Mass % ($\omega$)of FR | 15% | 15% | 15% |
| Mass % ($\omega$) of Br, Cl and P, respectively | 8.82% | 9.76% | 1.62% |
| $\rho_{\text{eff}}$*of Br, Cl and P, respectively | 93.5 mg/cm$^3$ | 103.5 mg/cm$^3$ | 17.2 mg/cm$^3$ |

*: $\rho_{\text{eff}}$ is the effective density calculated by $\rho_{\text{eff}}(\alpha) = \rho(\text{mixture}) \times \omega(\alpha)$.
For example, $\rho_{\text{eff}}(\text{Br}) = \rho(\text{mixture}) \times \omega(\text{Br}) = 1060 \times 8.82\% = 93.5$ mg/cm$^3$;
$\rho_{\text{eff}}(\text{ABS}) = \rho(\text{mixture}) \times \omega(\text{ABS}) = 1060 \times (1 - 15\%) = 901$ mg/cm$^3$.

### *3.1. ABS-FRs phantom*

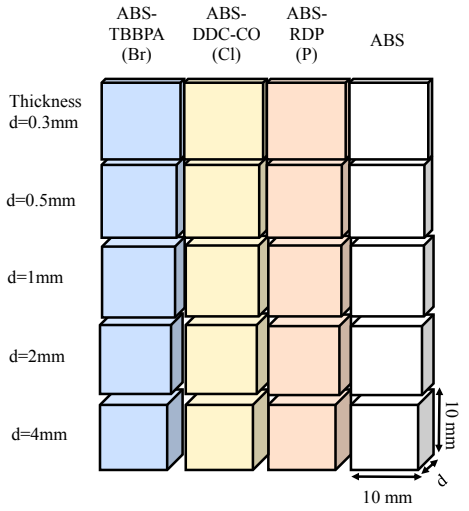


Figure 2: Illustration of the ABS-FR phantom used for spectral radiography imaging. Materials in the cubes are given in Table 1.

We simulate a phantom containing multiple polymer+FR mixtures. As mentioned above, ABS is a major component among the polymers used in electrical

and electronic equipments. Therefore, we selected it as the polymer material for investigation. We also chose three kinds of commonly used flame retardants, including the brominated, chlorinated and phosphorus FRs. They are respectively tetrabromobisphenol A (TBBPA), dechlorane plus (DDC-CO) and resorcinol bis(diphenyl phosphate) (RDP). Three ABS-FR materials were obtained by mixing each FR with ABS at mass percentage of 15%. Detailed information of these materials is summarized in Table 1.

The simulated phantom is composed of multiple cubes with height of 10 mm, width of 10 mm and different thicknesses. As shown in Figure 2, each column of cubes are of the same material (denoted on the top) and each row of cubes are of the same thickness (denoted on the left). Figure 3 plots the mass attenuation coefficients of the components contained in the phantom: ABS, Br, Cl and P, which will be used to distinguish different ABS-FR materials.

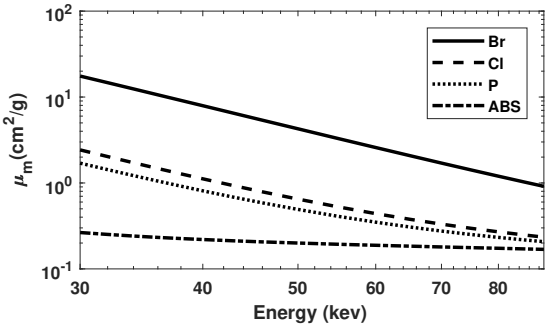


Figure 3: Mass attenuation coefficients ($\mu_{\mathrm{m}}$) of components (ABS, Br, Cl and P) within the detection energy range from 30 keV to 90 keV. $\mu_{\mathrm{m}}$ of ABS is calculated according to formula $\mu_{\mathrm{m}} = \sum_{\alpha} \omega_{\alpha} \mu_{\mathrm{m}\alpha}$, with $\omega_{\alpha}$ and $\mu_{\mathrm{m}\alpha}$ representing the weight fraction and mass attenuation coefficient of each element $\alpha$ of the compound. Data taken from [37].

From the decomposition method described in the above, the finally obtained $P_{\alpha}$ for material $\alpha$ is the line integral of material density $\rho_{\alpha}$ (Equation 3). In this case, with known thickness $d$ of each cube, theoretical values for $P_{\alpha}$ at position

Table 2: Theoretical values of $P_\alpha$ for each material. Material ABS has two columns: the first is *ABS pure*, which corresponds to the material of the $4th$ column of cubes in the phantom shown in Figure 2, and *ABS in mixture* corresponds to the ABS compound in the other cubes of Figure 2.

| Thickness (mm) | ABS pure ($mg/cm^2$) | ABS in mixtures ($mg/cm^2$) | Br in ABS-TBBPA ($mg/cm^2$) | Cl in ABS-DDC-CO ($mg/cm^2$) | P in ABS-RDP ($mg/cm^2$) |
|---|---|---|---|---|---|
| 0.3 | 31.80 | 27.03 | 2.81 | 3.11 | 0.52 |
| 0.5 | 53.00 | 45.05 | 4.68 | 5.18 | 0.86 |
| 1 | 106.00 | 90.10 | 9.35 | 10.35 | 1.72 |
| 2 | 212.00 | 180.20 | 18.70 | 20.70 | 3.44 |
| 4 | 424.00 | 360.40 | 37.40 | 41.40 | 6.88 |

$(sx, sy)$ of the transmitted image is given by

$$P_\alpha(sx, sy) = d(sx, sy) \times \rho_\alpha(sx, sy), \tag{6}$$

where $\rho_\alpha$ equals the effective density calculated in Table 1. Table 2 lists the theoretical values of $P_\alpha$ for materials ABS, Br, Cl and P at various thicknesses.

### *3.2. Acquisition parameters and system geometry*

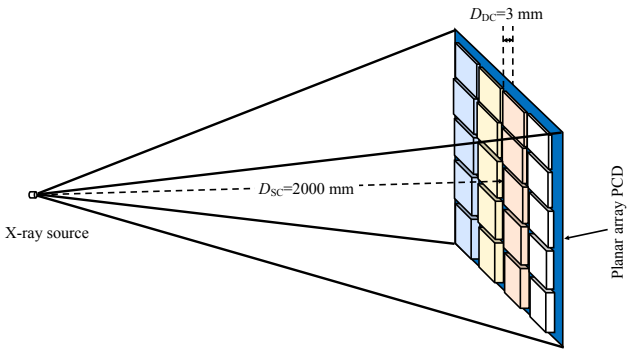


Figure 4: Scheme of spectral radiography system geometry. This figure is only a simplified schematic view of the simulation system where the dimensional information ($D_{SC}$, $D_{DC}$, size of phantom and detector) is not in real scale.

The simulated system used a point X-ray source of tungsten target material and the target angle was 17°. According to reference [38], tube voltage was set to be 100 kVp, tube current 15 mA and exposure time 1 s. The X-ray spectrum was computed based on Birch & Marshall model [39] without filtration. A 90×112 CdTe detector array with pixel size of 0.5 mm × 0.5 mm and thickness of 3 mm was simulated. Six energy bins were set to be evenly distributed from 30 keV to 90 keV. We assumed that the detector has ideal energy resolution, detector absorption efficiency was simulated as the fraction of photons absorbed by the detector material. The distance from X-ray source to phantom center was 2000 mm and the distance of detector to phantom center was 3 mm. Figure 4 is a schematic view of the simulated spectral radiography system. Photonic noises were simulated by simple Poisson distribution with means equaling the expected numbers of photons acquired for each energy bin [40, 41]. This process was implemented in Matlab using command *poissrnd*.

## 4. Simulation Results

We have simulated two sets of spectral radiography acquisition data: with and without photon noise. To better evaluate the performance of the proposed CPRD method, it was also compared with PRD method without classification.

### *4.1. Decomposition results of PRD method*

Regarding the components of the phantom, it is normal to consider a four basis material decomposition: ABS, Br, Cl and P. However, our experiment results show that P and Cl can barely be separated from each other since they have too close atomic number and hence close attenuation properties. Therefore, we decompose the radiographic images into three basis images corresponding to ABS, Br and Cl and expect that P will also be present in the Cl basis image. The patch size is set to be 2×2 pixels.

For simulated acquisition without noise, the relaxation parameter $r$ is set to 0 since it is not necessary to enforce smoothness within patches without noise. The decomposition results are shown in Figure 5(a). It is observed that:

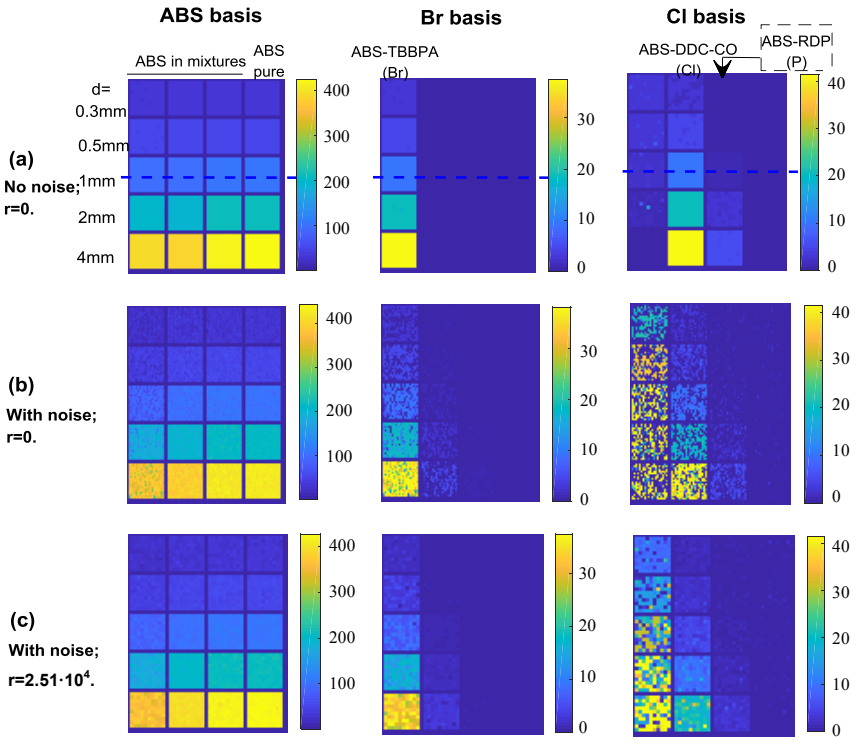


Figure 5: Decomposition results ($P_\alpha$) under different conditions using PRD method. (a): simulation without noise, $r = 0$; (b): simulation with Poisson noise, $r = 0$; (c): simulation with Poisson noise, $r = 2.51 \cdot 10^4$. The first column represents ABS basis, second column Br basis, and third column Cl basis image. The colorbars indicate decomposed $P_\alpha$ values in unit of mg/cm$^2$, whose true values are given in Table 2. The dash lines on images of (a) mark the position where 1-D profiles are plotted in later analysis.

- In the ABS basis image, all cubes are visible as expected, because ABS is present in both mixtures and pure ABS.

- In the Br basis image, the ABS-TBBPA cubes are well separated and highlighted with the $P_\alpha$ close to the true values, and no other FRs are present.

- In the Cl basis image, all the ABS-DDC-CO cubes are well highlighted as expected. At the same time, ABS-RDP is identified as Cl as expected, with $P_\alpha$ close to true values. However, for small thicknesses ($d \leq 2$ mm), a slight amount of ABS-TBBPA is misidentified as Cl.

Thus in the noise-free situation, ABS and Br can be well separated and identified. The determination performance of other FRs improves with the increase of object thickness: when $d = 4$ mm, the FRs containing Cl and P are present in the Cl basis image without cross-talk with the ABS-TBBPA material, one can further distinguish the two FRs according to their large density difference. In other words, if the thickness is known, the density can be used to identify the right material.

When Poisson noise is added, we need to reconsider the relaxation parameter $r$. $r$ is determined as $2.51 \cdot 10^4$ in this situation according to the L-curve criterion. Some details of $r$ selection using the L-curve method are introduced in the Appendix The decomposition results when $r = 0$ and $r = 2.51 \cdot 10^4$ are shown in Figure 5(b) and (c). It can be seen that when $r = 0$ (without regularization), the ABS-TBBPA cubes and ABS-DDC-CO cubes appear in both Br basis image and Cl basis image, making them impossible to be distinguished. Moreover, the decomposed images suffer from heavy noise. When the relaxation parameter was set to $r = 2.51 \cdot 10^4$, the obtained images are less noisy than those in the former case, however, the separation of different materials is not enhanced. Another method is thus necessary.

*4.2. Decomposition results with the new CPRD method*

Instead of the 3-material (ABS, Br and Cl) decomposition using PRD method, we perform two independent decompositions with two groups of basis materials, *group 1* is ABS + Br, and *group 2* ABS + Cl. We give up a third group of ABS + P because it generates comparable cost function values with *group 2*, resulting in severe cross-talk between Cl and P. With the selected two groups of decomposition, by comparing the cost function values (fval1 and fval2) at the end of each decomposition, one of the two decompositions is chosen for a given patch. For example, if fval1<fval2, we choose the results of the decomposition that decomposes the data into ABS and Br, consequently, the values of Cl in this patch will be set to 0. After all patches being considered, full images of ABS, Br and Cl are obtained. Figure 6 shows the decomposition results of CPRD method and a reference method in the same condition as that in the above method without classification. The reference method employs a widely used least squares error objective function to solve the decomposition problem pixel by pixel [42].

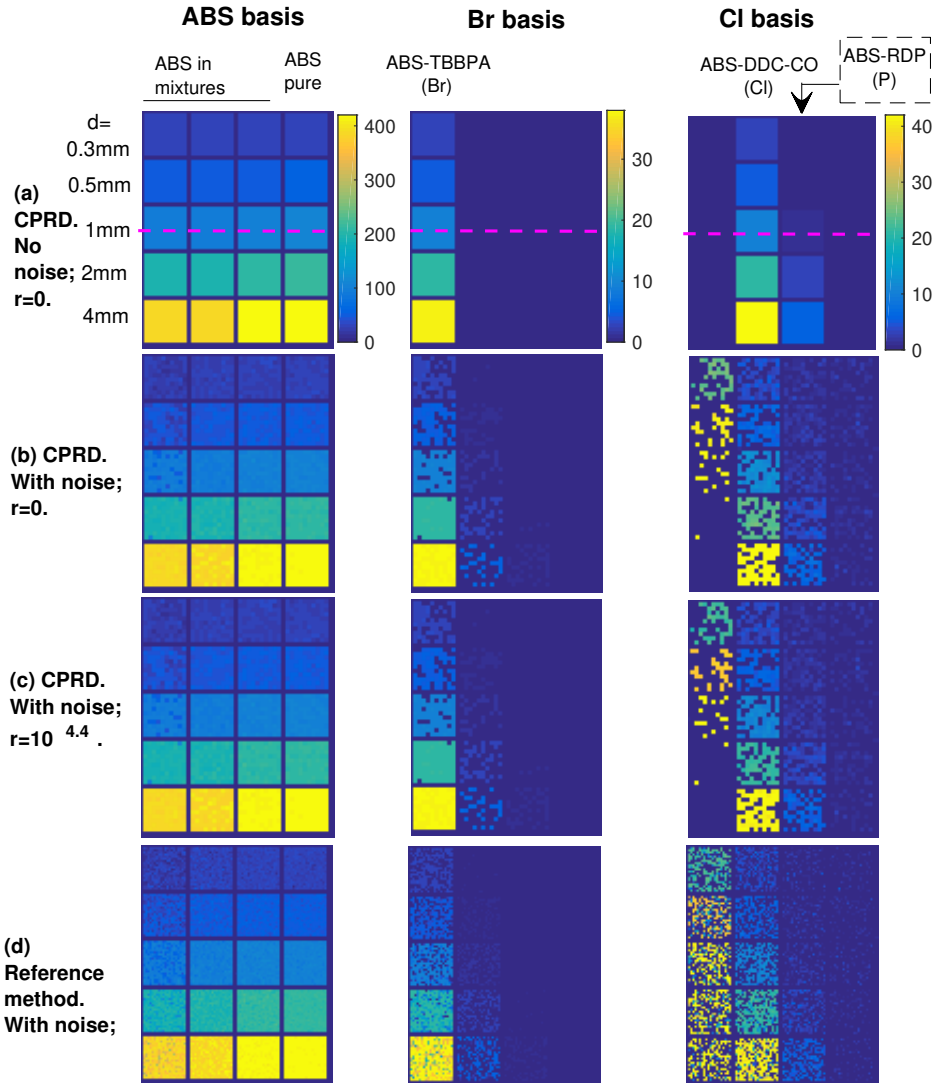


Figure 6: Decomposition results under different conditions using CPRD method and reference method: (a) CPRD method, simulation without noise, $r = 0$; (b) CPRD method, simulation with Poisson noise, $r = 0$; (c) CPRD method, simulation with Poisson noise, $r = 2.51 \cdot 10^4$; (d) reference method, simulation with Poisson noise. The first column represents ABS basis, second column Br basis, and third column Cl basis image. Each column shares the same colorbar which indicates decomposed $P_\alpha$ values in unit of mg/cm$^2$, whose values are given in Table 2. The dash lines on images of (a) mark the position where 1-D profiles are plotted in later analysis.

In the noise-free condition (Figure 6(a)), FRs containing ABS and Br are identified respectively by CPRD method in the ABS and Br basis images as expected. Meanwhile, only the cubes of FR materials containing Cl and P appear in the Cl basis image, but they have significant density difference for cubes with the same thickness, therefore, they can be easily distinguished by the observer even if the concentration of FRs or thickness of cubes changes more or less.

In the presence of Poisson noise, Figure 6(b) shows the decomposition results of CPRD method when $r = 0$ (without regularization). Noise can be observed in decomposition images, however, material separation is better than with PRD method (compared with Figure 5): only few pixels containing Cl are misidentified in the Br basis image and vice versa. The cross-talk situation improves with the increase of thickness. In Figure 6(c), when $r = 2.51 \cdot 10^4$ (with regularization), the material separation is further enhance to some extent compared with Figure 6(b): less pixels of ABS-DDC-CO cubes appear in the Br basis image, and only the ABS-DDC-CO and ABS-RDP cubes are highlighted in the Cl image when $d = 2$ mm or 4 mm, like the results in noise-free case. In contrast, the reference method fails to separate Br and Cl. As can be seen in 6(d), the cubes containing Br also appear in the Cl basis image, no matter what thickness the sample has. Therefore, the CPRD method outperforms the reference method for material decomposition.

A more quantitative comparison is done in Figure 7, where the profiles of computed $P_\alpha$ with PRD and CPRD method are plotted together with the theoretical values (along dash lines in both Figure 5 and 6). It is observed that the CPRD method yields closer results to true values with respect to the PRD method especially for the Cl basis curve, where ABS-TBBPA cubes are mistaken as Cl containing FR by PRD method. It is noteworthy that the theoretical values of $P_\alpha$ for the ABS-RDP cube in the Cl basis image are set to 1.72mg/cm$^2$ (corresponding to Table 2, the $P_\alpha$ of P in ABS-RDP with thickness of 1 mm) instead of 0, because we expect that P will appear in the Cl basis image.

So, the CPRD method has better decomposition ability than PRD for the

sorting application, no matter when Poisson noise is or is not present. ABS and Br containing FR can be identified in their corresponding basis images. Furthermore, when the cube thickness is increased to 2 mm or 4 mm, the decomposition results of Poisson noise condition become much closer to those of noise-free condition, where ABS and the FRs containing Br, Cl and P can be identified simultaneously.

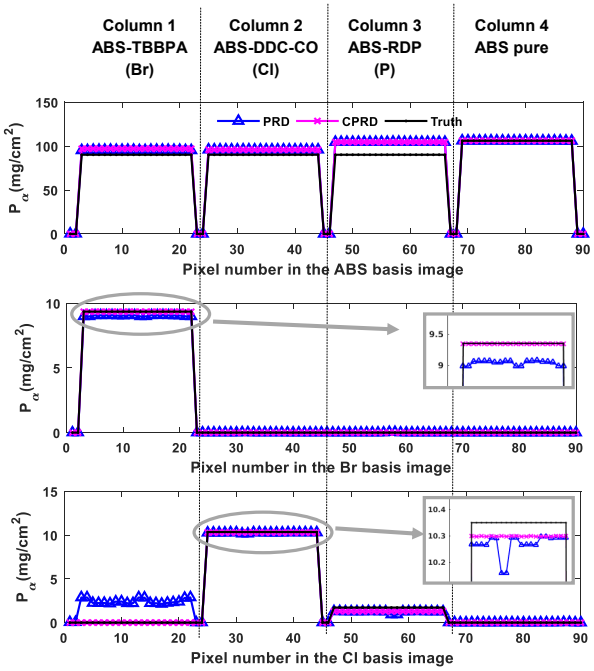


Figure 7: Performance comparison of PRD and CPRD methods in noise-free condition: 1-D profiles along the dash lines in Figures 5 and 6. ABS basis (top), Br basis (middle) and Cl basis (bottom). Black curves with point marker represent the theoretical density integrals of basis materials ($P_\alpha$ for thickness of 1 mm in Table 2)for perfect decomposition. Blue curves with triangle marker represent the calculated values using PRD method and the magenta curves with cross marker using CPRD method.

## 5. Preliminary experimental results

In order to evaluate the performance of our proposed method on physical data, we carried out radiography measurements using a CdTe photon-counting

detector from Detection Technology company. The detector has linear array structure with 256 detector pixels, each pixel is of 0.8 mm pitch size. The detector provides the possibility of setting 64 uniformly distributed energy bins between 20 keV and 160 keV. Considering our tube voltage of 110kVp for this experiment, we used data of the first 36 bins (20 keV to 110 keV) to perform material decomposition. As shown in Figure 8, the object being scanned is composed of 5 materials: polyvinyl chloride (PVC), ABS with 20% Br, ABS with 5% Cl, polypropylene (PP) with 20% $CaCO_3$, and ABS pure. Acquisition parameters were set as: tube current 200 $\mu$A, exposure time 100 ms, source to object distance 46 cm and object to detector distance 13 cm.

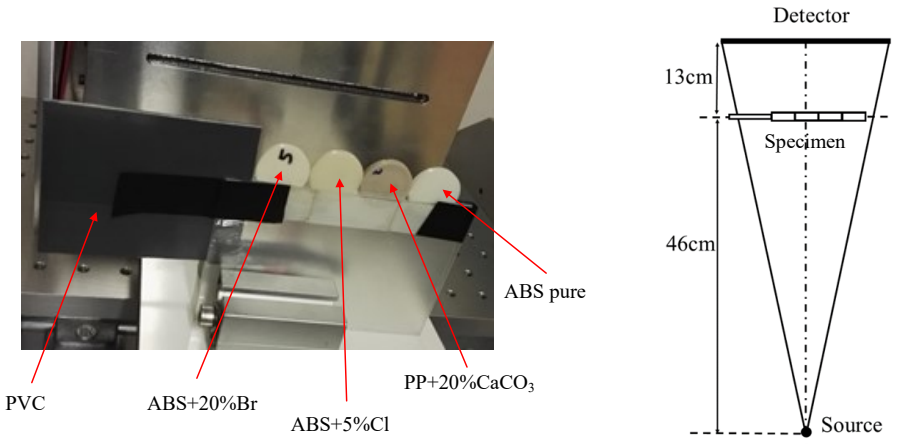


Figure 8: Illustration of experimental specimen (left) and system geometry (right).

Because of the linear structure of the detector, we have acquired single line data of 256 pixels. Therefore, the patchwise regularization, which requires 2 dimensional gradient, can not be directly applied. We hence adjusted our CPRD method by removing the regularization term and using patch size of 1x1 for experimental validation. 3 groups of basis materials were selected: *group 1* "ABS + Br", *group 2* "ABS + Cl", *group 3* "ABS + Ca".

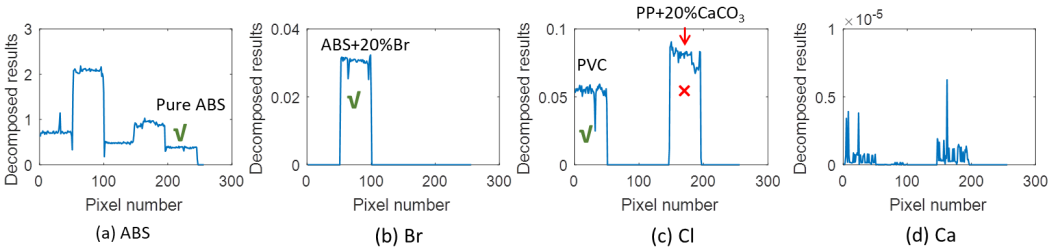


Figure 9: Decomposition results of ABS (a), Br (b), Cl (c) and Ca (d). The green check mark indicates a good decomposition while the red cross mark indicates a false decomposition.

The decomposition results are shown in Figure 9. It can be observed that all 5 materials are visible in Figure 9(a), since they either really contain ABS or contain components like PVC or PP that have similar attenuation properties to ABS. The pure ABS curve appears only in Figure 9(a), which indicates a good separation from other basis materials. In Figure 9(b), component Br is well discriminated. In Figure 9(c) the Cl component in PVC is well identified. However, a mistaken peak of PP with 20% $CaCO_3$ also appears, indicating that Ca probably cannot be separated from Cl. Also, the sample containing 5% Cl remains undetected.

In short, the proposed method achieves to identify ABS, Br as well as Cl with relatively higher concentration, but materials with close atom numbers, such as Ca and Cl remain unseparated.

## 6. Discussions

We have proposed a classification-based material decomposition method, which achieves to identify several different plastic materials in both simulation and experimental validations. There are several parameters and factors that may influence the decomposition performance as discussed below.

**Choice of basis materials.** During simulation, we have found that using basis materials that have close chemical formulas to those actually present in the object can improve the decomposition performance. For example, using the same simulation data with Poisson noise, besides the above presented results, we

have also performed a 3-group decomposition with basis materials like, *Group 1* (ABS + TBBPA), *Group 2* (ABS + DDC-CO) and *Group 3* (ABS + RDP). The results showed that with cube thickness of 2 mm and 4 mm, ABS and three FRs can be identified according to their corresponding decomposition image. That is to say, DDC-CO and RDP can be distinguished from each other directly by decomposing them into their corresponding basis, instead of by their density difference in the same basis (Cl) image, as described in the above results of the CPRD method. We have not chosen these groups of basis materials with better performance because they are too specific. However, for the application where the components of object are well known, appropriate choice of basis materials can yield better decomposition performance.

**Patch size.** In the present study, we have used a patch size of $2 \times 2$ pixels. To investigate the influence of patch size on decomposition performance, we plot in Figure 10 the curve of quantification error versus patch size, where quantification error represents root-mean-square-error (RMSE) of decomposed Br basis image. As observed, $2 \times 2$ patch size gives the smallest RMSE. Quantification error increases when patch size is larger than 2. This could be caused by the fact that large patch size results in over-smoothed image [43]. As a result, since there exist sharp grid-like edges throughout our entire image, over-smoothing of these edges leads to larger quantification errors.

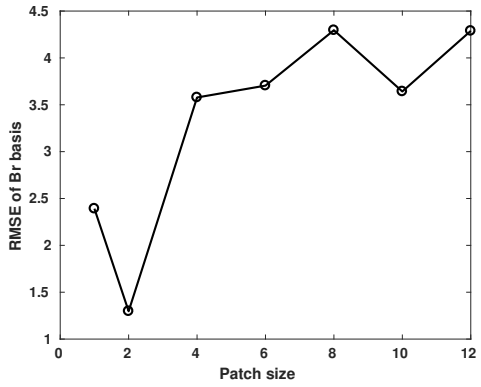


Figure 10: RMSE of quantified Br densities versus patch size.

**Relaxation parameter $r$.** Although the separation between materials is not enhanced (for PRD method) or slightly enhanced (for CPRD method) by choosing $r$ according to L-curve method, it is still meaningful that noise (indicated by the variation of pixel values) of decomposition image can be decreased, which is obvious in Figure 5. We have applied L-curve method to certain region of the radiographic images, and used the same $r$ for all patches. However, $r$ should perhaps be changed for different patches if the signal-to-noise ratio varies. Therefore, further improvement could be achieved by tuning the relaxation parameter in each patch.

**Placement of energy bins.** In the present work, we have used 6 uniformly distributed bins within detecting energy range to evaluate the performance of our proposed method in a general way. However, according to some researches [44, 45], appropriate selection of energy bins may have large influence on decomposition performance, especially when the total number of bins are small. In Figure 11(b), we demonstrate the decomposition results using a different strategy to place 6 energy bins. More bins were placed in lower energy on purpose since lower energy carries more material-differentiation information. We can observe performance improvement compared to Figure 11(a). From the ROI marked by the red circles, Br was better recognized with less cross-talk in Cl basis. Moreover, the calculated RMSE of Br basis image decreased from 1.23 to 0.88, indicating less quantification errors.

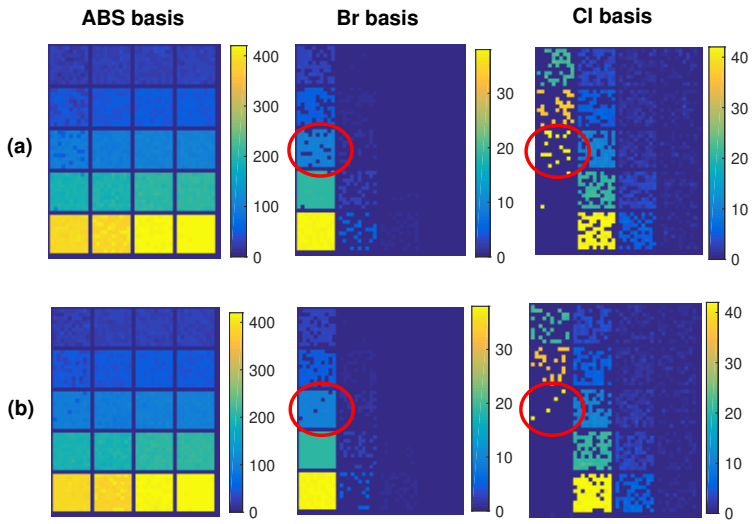


Figure 11: Comparison of decomposition results using different strategies of selecting energy bins. (a) 6 energy bins are uniformly distributed between 30keV and 90 keV, which is the same as Figure 6 (c). (b) More bins were placed in lower energy range as follows: 30 - 34, 35 - 41, 42 - 50, 51 - 61, 62 - 74 and 75 - 90 keV.

**Detector response.** In the present work, simulation validation only considers the absorption efficiency of the detector. However, in reality, photon counting detector's response function can be modeled by mixture of Gaussian functions allowing taking into account several artifacts such as electronic noise, charge sharing, pulse pile-up, K-escape and Compton scattering [46]. Electronic noise is an important factor that limits the energy resolving capability of detector, it results in spectral resolution degradation and potential false counts especially at low energy. [47]. Charge sharing effect occurs when the charge cloud generated from X-ray interaction is shared by neighboring pixels and results in two or more counts in several pixels and with lower energies. This effect is especially serious when pixel size is less than 0.5 mm [48]. Pulse pile-up takes place at high count rate; two nearly simultaneously incident photons are counted as one, leading to loss of count and wrong recorded energy. This effect can be reduced by controlling incident count rate [47]. K-escape effect

is due to the characteristic X-rays induced by photoelectric effect. It can lead to different consequences: the recorded energy is lowered by K-shell energy, or two counts are generated, or still pile-up effect is induced [49].Compton scattering refers to Compton effect-induced scattered photons that are detected by an adjacent pixel or leave the PCD completely, resulting in long tail in lower energy. All these effects lead to distorted detector response and reduction of energy resolution. The degraded performance of material decomposition caused by discrepancy between theoretical and measured data can be addressed by two approaches. The first one is to characterize detector response by synchrotron radiation, radioactive isotopes or x-ray fluorescence [50], and then incorporate this information into material decomposition [51]. The second one is to calibrate material's linear attenuation coefficient by scanning samples with known components and thickness, so as to take into consideration the influence of detector response. The second approach is more flexible, easy to accomplish and efficient according to our preliminary test on experimental data. Though this strategy was not used for the demonstrated results here, we can still observe pretty good decomposition performance, indicating that our proposed method is able to process real experimental data.

There are certain limitations of the proposed method. Firstly, the CPRD method is not enough robust to noise when the object thickness is small. Secondly, the decomposition of the two FRs with similar properties (DDC-CO and RDP), even in the noise-free case, depends on their density difference in the Cl image. Therefore, in case where the thickness information of objects is unknown, or the two materials overlap in the X-ray direction, the decomposed density will be largely influenced, yielding the materials indistinguishable. Although an optional solution has been mentioned in the above, which consists in using directly DDC-CO and RDP as basis materials, but in a more generalized situation, close materials are still hard to be distinguished. Thirdly, the proposed CPRD method performs several decompositions into different groups of basis materials and then uses a classification technique to decide the right type of material. Although a decreased number of basis materials in each group re-

duces the running time of each decomposition, compared with a normal one with multiple basis materials, but on the other hand, the computation time can be increased because of extra decomposition procedures. For instance, in the present study, the 2-group (two basis materials in each group) CPRD decomposition has about 36% longer running time than the 3-material PRD decomposition.

## 7. Conclusions

To investigate the ability of PCD-based spectral radiography for plastic sorting, we have proposed a classification-based decomposition method and evaluated its performance through both simulation and experimental validations. The simulation results showed that the proposed CPRD method is able to distinguish ABS and the FRs containing Br, Cl and P at the same time if the cube thickness is as large as 2 mm or 4 mm. Moreover, the quantified material densities agree well with theoretical values. Experimental validations further confirm that ABS, Br and Cl can be separated from each other, but that materials with close atom numbers, i.e. Ca and Cl remain unseparated. Despite some limitations, our results suggest the possibility that PCD-based spectral radiography can be used to sort different types of plastic materials.

In addition to plastic sorting presented in the present work, the proposed method can be readily applied to other applications such as industrial and medical ones. For example, in explosive detection, the explosive substances have close X-ray attenuation properties with some common materials such as sugar and polyethylene, a spectral radiography scan followed by the CPRD decomposition may improve their separation. Furthermore, the proposed method can be adapted to spectral photon-counting CT by adding a reconstruction step to transform the projection density integral information into cross-sectional density distributions. Thus spectral CT inspections could benefit from the proposed method too, such as abdominal imaging and atherosclerosis imaging, where material-specific imaging is of great importance for characterizing lesions or high risk plaques.

## Appendix A. Determination of $r$ with L-curve method

The L-curve is a log-log plot of the norm of a regularized solution versus the norm of the corresponding residual, where the "corner" of the curve corresponds to the selected relaxation parameter [52]. The solution and residual norms correspond to the objective function value and $R(P_\alpha^C)$ value in Equation 4. We choose a region of interest on the radiographic image for the determination of $r$, which is shown in Figure A1.

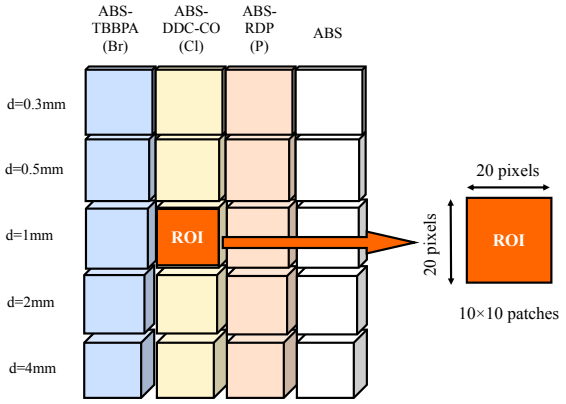


Figure A1: Illustration of ROI for the determination of $r$.

The ROI contains 20×20 pixels. Given that the patch size is 2×2, there are 10 ×10=100 patches within the ROI. For a given $r$, we define the solution norm and residual norm as the average values calculated over the 100 patches. We plot the L-curve with $r$ varying from $10^{-10}$ to $10^{10}$, as shown in Figure A2 (a). It is observed that the "corner" exists between $r = 10^4$ and $r = 10^5$. Furthermore, by plotting the same curve for a set of $r$ between $10^4$ and $10^5$, we have the curves shown in Figure A2(b). From this figure, we select $r = 2.51 \cdot 10^4$ as the relaxation parameter for all patches.

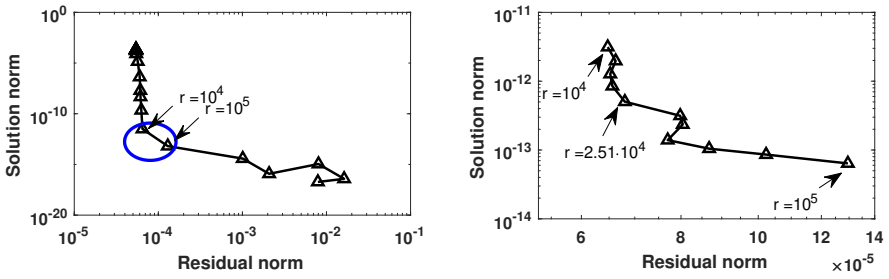


(a) (b)

Figure A2: The L-curve as a function of residual norm for different values of the relaxation parameter $r$ (a), and a magnified view of the blue circle region, where $r$ varies from $10^4$ to $10^5$ (b).

## References


[1] W. R. Brody, D. M. Cassel, F. G. Sommer, L. Lehmann, A. Macovski, R. E. Alvarez, N. J. Pelc, S. J. Riederer, A. L. Hall, Dual-energy projection radiography: initial clinical experience, American Journal of Roentgenology 137 (2) (1981) 201–205.

[2] P. Vock, Z. Szucs-Farkas, Dual energy subtraction: principles and clinical applications, European journal of radiology 72 (2) (2009) 231–237.

[3] W. R. Brody, G. Butt, A. Hall, A. Macovski, A method for selective tissue and bone visualization using dual energy scanned projection radiography, Medical physics 8 (3) (1981) 353–357.

[4] F. Manji, J. Wang, G. Norman, Z. Wang, D. Koff, Comparison of dual energy subtraction chest radiography and traditional chest x-rays in the detection of pulmonary nodules, Quantitative imaging in medicine and surgery 6 (1) (2016) 1–5.

[5] B. Zhou, Y. Jiang, D. Wen, R. C. Gilkeson, J. Hou, D. L. Wilson, Visualization of coronary artery calcium in dual energy chest radiography

using automatic rib suppression, in: Medical Imaging 2018: Image Processing, Vol. 10574, International Society for Optics and Photonics, 2018, p. 105740E.

[6] S. Singh, M. Singh, Explosives detection systems (eds) for aviation security, Signal processing 83 (1) (2003) 31–55.

[7] J. Pashby, S. Glenn, C. Divin, H. Martz, Radiation detection and dual-energy x-ray imaging for port security, Tech. rep., Lawrence Livermore National Lab.(LLNL), Livermore, CA (United States) (2017).

[8] D. Lee, J. Lee, J. Min, B. Lee, B. Lee, K. Oh, J. Kim, S. Cho, Efficient material decomposition method for dual-energy x-ray cargo inspection system, Nuclear Instruments and Methods in Physics Research Section A: Accelerators, Spectrometers, Detectors and Associated Equipment 884 (2018) 105–112.

[9] F. Montagner, V. Kaftandjian, P. Duvauchelle, N. Pedoussaut, A. Bourely, Dual energy radioscopy applied to waste sorting, in: European Conference on Non Destructive Testing, 2014.

[10] S. P. Gundupalli, S. Hait, A. Thakur, A review on automated sorting of source-separated municipal solid waste for recycling, Waste Management 60 (2017) 56–74.

[11] J. Duvillier, M. Dierick, J. Dhaene, D. Van Loo, B. Masschaele, R. Geurts, L. Van Hoorebeke, M. N. Boone, Inline multi-material identification via dual energy radiographic measurements, NDT & E International 94 (2018) 120–125.

[12] K. Ogawa, T. Kobayashi, F. Kaibuki, T. Yamakawa, T. Nagano, D. Hashimoto, H. Nagaoka, Development of an energy-binned photon-counting detector for x-ray and gamma-ray imaging, Nuclear Instruments and Methods in Physics Research Section A: Accelerators, Spectrometers, Detectors and Associated Equipment 664 (1) (2012) 29–37.

[13] E. Babichev, S. Baru, D. Grigoriev, V. Leonov, V. Oleynikov, V. Porosev, G. Savinov, Photon counting detector for the personal radiography inspection system "sibscan", Nuclear Instruments and Methods in Physics Research Section A: Accelerators, Spectrometers, Detectors and Associated Equipment 845 (2017) 499–502.

[14] E. Gimenez, V. Astromskas, I. Horswell, D. Omar, J. Spiers, N. Tartoni, Development of a schottky cdte medipix3rx hybrid photon counting detector with spatial and energy resolving capabilities, Nuclear Instruments and Methods in Physics Research Section A: Accelerators, Spectrometers, Detectors and Associated Equipment 824 (2016) 101–103.

[15] P. Zambon, V. Radicci, P. Trueb, C. Disch, M. Rissi, T. Sakhelashvili, M. Schneebeli, C. Broennimann, Spectral response characterization of cdte sensors of different pixel size with the ibex asic, Nuclear Instruments and Methods in Physics Research Section A: Accelerators, Spectrometers, Detectors and Associated Equipment 892 (2018) 106–113.

[16] G. Beldjoudi, V. Rebuffel, L. Verger, V. Kaftandjian, J. Rinkel, An optimised method for material identification using a photon counting detector, Nuclear Instruments and Methods in Physics Research Section A: Accelerators, Spectrometers, Detectors and Associated Equipment 663 (1) (2012) 26–36.

[17] E. e. Fredenberg, Spectral and dual-energy x-ray imaging for medical applications, Nuclear Instruments and Methods in Physics Research Section A: Accelerators, Spectrometers, Detectors and Associated Equipment 878 (2018) 74–87.

[18] X. Xu, Y. Xing, S. Wang, L. Zhang, Systematic implementation of spectral ct with a photon counting detector for liquid security inspection, Nuclear Instruments and Methods in Physics Research Section A: Accelerators, Spectrometers, Detectors and Associated Equipment 893 (2018) 99–108.

[19] T. Maruhashi, H. Morita, M. Arimoto, J. Kataoka, K. Fujieda, H. Nitta, H. Ikeda, H. Kiji, Evaluation of a novel photon-counting ct system using a 16-channel mppc array for multicolor 3-d imaging, Nuclear Instruments and Methods in Physics Research Section A: Accelerators, Spectrometers, Detectors and Associated Equipment 936 (2018) 5–9.

[20] S. Si-Mohamed, D. Bar-Ness, M. Sigovan, D. P. Cormode, P. Coulon, E. Coche, A. Vlassenbroek, G. Normand, L. Boussel, P. Douek, Review of an initial experience with an experimental spectral photon-counting computed tomography system, Nuclear Instruments and Methods in Physics Research Section A: Accelerators, Spectrometers, Detectors and Associated Equipment 873 (2017) 27–35.

[21] E. Roessl, R. Proksa, K-edge imaging in x-ray computed tomography using multi-bin photon counting detectors, Physics in medicine and biology 52 (15) (2007) 4679–4696.

[22] J. Schlomka, E. Roessl, R. Dorscheid, S. Dill, G. Martens, T. Istel, C. Bäumer, C. Herrmann, R. Steadman, G. Zeitler, et al., Experimental feasibility of multi-energy photon-counting k-edge imaging in pre-clinical computed tomography, Physics in medicine and biology 53 (15) (2008) 4031–4047.

[23] H. Q. Le, S. Molloi, Least squares parameter estimation methods for material decomposition with energy discriminating detectors, Medical physics 38 (1) (2011) 245–255.

[24] A. M. Alessio, L. R. MacDonald, Quantitative material characterization from multi-energy photon counting ct, Medical physics 40 (3).

[25] D. Zeng, Y. Gao, J. Huang, Z. Bian, H. Zhang, L. Lu, J. Ma, Penalized weighted least-squares approach for multienergy computed tomography image reconstruction via structure tensor total variation regularization, Computerized Medical Imaging and Graphics 53 (2016) 19–29.

[26] B. Xie, T. Su, V. Kaftandjian, P. Niu, F. Yang, M. Robini, Y. Zhu, P. Duvauchelle, Material decomposition in x-ray spectral ct using multiple constraints in image domain, Journal of Nondestructive Evaluation 38 (1) (2019) 16.

[27] T. Su, V. Kaftandjian, P. Duvauchelle, Y. Zhu, A spectral x-ray ct simulation study for quantitative determination of iron, Nuclear Instruments and Methods in Physics Research Section A: Accelerators, Spectrometers, Detectors and Associated Equipment 894 (2018) 39–46.

[28] T. Su, Quantitative material decomposition methods for x-ray spectral ct, Ph.D. thesis, Insa Lyon (2018).

[29] J. Beigbeder, D. Perrin, J.-F. Mascaro, J.-M. Lopez-Cuesta, Study of the physico-chemical properties of recycled polymers from waste electrical and electronic equipment (weee) sorted by high resolution near infrared devices, Resources, Conservation and Recycling 78 (2013) 105–114.

[30] J. Cui, E. Forssberg, Mechanical recycling of waste electric and electronic equipment: a review, Journal of hazardous materials 99 (3) (2003) 243–263.

[31] J. R. Peeters, P. Vanegas, L. Tange, J. Van Houwelingen, J. R. Duflou, Closed loop recycling of plastics containing flame retardants, Resources, Conservation and Recycling 84 (2014) 35–43.

[32] H. Fromme, G. Becher, B. Hilger, W. Völkel, Brominated flame retardants–exposure and risk assessment for the general population, International journal of hygiene and environmental health 219 (1) (2016) 1–23.

[33] T. Su, V. Kaftandjian, P. Duvauchelle, Y. Zhu, Plastic sorting by x-ray radioscopy with photon counting detector, in: 12th European conference on Non-Destructive Testing, 2018.

[34] T. Su, V. Kaftandjian, P. Duvauchelle, P. Douek, Y. Zhu, Quantitative material decomposition method for spectral ct imaging, in: 7th Conference on Industrial Computed Tomography, 2017.

[35] T. Su, V. Kaftandjian, P. Duvauchelle, Y. M. Zhu, Material decomposition for spectral ct: application to calcium and iodine identification, in: 2017 IEEE Nuclear Science Symposium and Medical Imaging Conference, 2017.

[36] P. Duvauchelle, N. Freud, V. Kaftandjian, D. Babot, A computer code to simulate x-ray imaging techniques, Nuclear Instruments and Methods in Physics Research Section B: Beam Interactions with Materials and Atoms 170 (1-2) (2000) 245–258.

[37] J. Hubbell, S. Seltzer, Tables of x-ray mass attenuation coefficients and mass energy-absorption coefficients (version 1.4), National Institute of Standards and Technology, Gaithersburg, MD.

[38] F. Montagner, Nouvelles méthodes de tri des déchets par rayons x, Ph.D. thesis, Lyon, INSA (2012).

[39] R. Birch, M. Marshall, Computation of bremsstrahlung x-ray spectra and comparison with spectra measured with a ge (li) detector, Physics in Medicine & Biology 24 (3) (1979) 505–517.

[40] B. R. Whiting, P. Massoumzadeh, O. A. Earl, J. A. O'Sullivan, D. L. Snyder, J. F. Williamson, Properties of preprocessed sinogram data in x-ray computed tomography, Medical physics 33 (9) (2006) 3290–3303.

[41] J. Ma, Z. Liang, Y. Fan, Y. Liu, J. Huang, W. Chen, H. Lu, Variance analysis of x-ray ct sinograms in the presence of electronic noise background, Medical physics 39 (7Part1) (2012) 4051–4065.

[42] S. Lee, C. Yu-Na, K. Hee-Joung, Quantitative material decomposition using spectral computed tomography with an energy-resolved photon-counting detector, Physics in Medicine & Biology 59 (18) (2014) 5457.

[43] C. Zhang, T. Zhang, M. Li, C. Peng, Z. Liu, J. Zheng, Low-dose ct reconstruction via l1 dictionary learning regularization using iteratively reweighted least-squares, in: Biomedical engineering online, 2016.

[44] S. Leng, L. Yu, J. Wang, J. G. Fletcher, C. A. Mistretta, C. H. McCollough, Noise reduction in spectral ct: Reducing dose and breaking the trade-off between image noise and energy bin selection, Medical physics 38 (9) (2011) 4946–4957.

[45] A. S. Wang, N. J. Pelc, Optimal energy thresholds and weights for separating materials using photon counting x-ray detectors with energy discriminating capabilities, in: Medical Imaging 2009: Physics of Medical Imaging, Vol. 7258, International Society for Optics and Photonics, 2009, p. 725821.

[46] T. G. Schmidt, Ct energy weighting in the presence of scatter and limited energy resolution, Medical Physics 37 (3) (2010) 1056–1067.

[47] E. Fredenberg, M. Lundqvist, B. Cederström, M. Åslund, M. Danielsson, Energy resolution of a photon-counting silicon strip detector, Nuclear Instruments and Methods in Physics Research Section A: Accelerators, Spectrometers, Detectors and Associated Equipment 613 (1) (2010) 156 – 162.

[48] L. Ren, B. Zheng, H. Liu, Tutorial on x-ray photon counting detector characterization., Journal of X-ray science and technology 26 1 (2017) 1–28.

[49] K. Taguchi, J. S. Iwanczyk, Vision 20/20: Single photon counting x-ray detectors in medical imaging, Medical physics 40 (10).

[50] H. Ding, H.-M. Cho, W. C. Barber, J. S. Iwanczyk, S. Molloi, Characterization of energy response for photon-counting detectors using x-ray fluorescence, Medical Physics 41 (12) (2014) 121902.

[51] J. Liu, H. Gao, Material reconstruction for spectral computed tomography with detector response function, Inverse Problems 32 (11) (2016) 114001.

[52] P. C. Hansen, The l-curve and its use in the numerical treatment of inverse problems, Computational Inverse Problems in Electrocardiology (2001) 119–142.